Optics and Laser Technology 112 (2019) 107–116

Contents lists available at ScienceDirect

Optics and Laser Technology

journal homepage: www.elsevier.com/locate/optlastec

Full length article

Effect of Sm^{3+} substitution on the structural and magnetic properties of Ni-Co nanoferrites

M.K. Kokare[a], Nitin A. Jadhav[b], Vijay Singh[c], S.M. Rathod[d,*]

[a] Department of Physics, Tuljaram Chaturchand College, Baramati, Pune, India
[b] Vidya Pratishthans Kamalnayan Bajaj Institute of Engineering and Technology, Baramati, Pune, India
[c] Department of Chemical Engineering, Konkuk University, Seoul 05029, Republic of Korea
[d] Department of Physics, A.G. College, Pune, India

HIGHLIGHTS

- Sm^{3+} incorporation maintained single phase cubic structure of Ni-Co ferrite.
- Lattice strain with Sm^{3+} was increased.
- FESEM micrographs exhibited agglomeration of grains with size varying from 40–60 nm.
- Saturation magnetization upto x = 0.1 was decreased while for x = 0.125 it increases.
- Observed Canting effect reveal the non-collinear structure.

ARTICLE INFO

Keywords:
Nanoferrites
Samarium
Cation distribution
Agglomeration
Saturation Magnetization
Magneton number

ABSTRACT

Samarium doped nanoferrites $Ni_{0.5}Co_{0.5}Sm_xFe_{2-x}O_4$ with (x = 0.00, 0.025, 0.05, 0.075, 0.10, 0.125) samples were prepared by using auto-combustion route. XRD pattern analysis confirmed the single-phase cubic spinel structure with no evidence of secondary phase. It is observed that, the lattice constant decreased from 8.342 Å (x = 0) to 8.321 Å (0.100) and again increased to 8.370 for x = 0.125. The crystallite size and particle size indicate the nano sized nature of the prepared ferrites. Crystalite size varies nonlinearly between 33 nm and 25 nm with addition of Sm^{3+} content in Ni-Co nanoferrites. The agglomerated grain structure revealed the high surface interaction among magnetic nanoparticles. FTIR spectra revealed the characteristics features of ferrite skeleton formation. The saturation magnetization, coercivity and remanence magnetization are found to decreases with the substitution of Sm^{3+} ions.

1. Introduction

Spinel ferrite having general formula MFe_2O_4 exhibits interesting property of magnetic conductor and electrical insulator. These properties are governed by type of the cations and its distribution over the tetrahedral and octahedral sub-lattices. The characteristic properties of the nanoferrites depend on the method, the condition of preparation, chemical composition, sintering temperature etc. [1]. Several chemical methods such as sol-gel, co-precipitation, combustion technique, etc. have been used for the preparation of stoichiometric and chemically pure nano ferrite materials [2]. High saturation magnetization, high permeability and a remarkably high electrical resistivity at high frequency are some of the excellent features of spinel ferrites [3,4].

The properties of spinel ferrites in nano-scale differ significantly from those of the bulk material. Spinel ferrite nanoparticles have diverse applications in home appliances, electronic products, communication, recording media, radio, television, microwave, etc. [5,6]. In addition to above, they are used in a variety of areas such as magnetic data storage, microwave absorbing materials, targeted release of drugs, water purification, etc. [7,8]. Use of rare earth doped magnetic nanoparticles is found to be more efficient to get the relief the acute pains and uneasiness due to injuries and diseases [9].

Nickel-cobalt mixed spinel ferrite is the magnetic material which is widely used in the variety of high frequency applications. In the literature, magnetic, electrical and dielectric properties of nanocrystalline mixed Ni-Co ferrites have been reported [10]. Also, the magnetic properties of Ni-Co ferrites were explored by researchers [11,12]. Recently, many researchers have investigated the properties of spinel

* Corresponding author.
E-mail address: sopan.rathod@mesagc.org (S.M. Rathod).

https://doi.org/10.1016/j.optlastec.2018.10.045
Received 27 September 2018; Accepted 20 October 2018

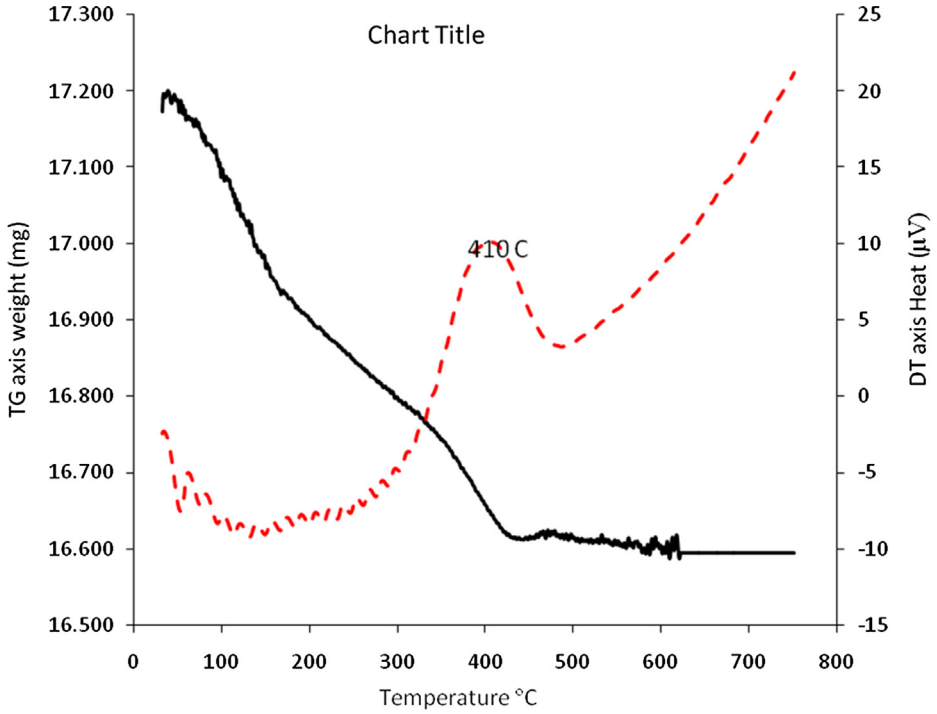

Fig. 1. TGA-DTA of $Ni_{0.5}Co_{0.5}Sm_{0.1}Fe_{1.9}O_4$.

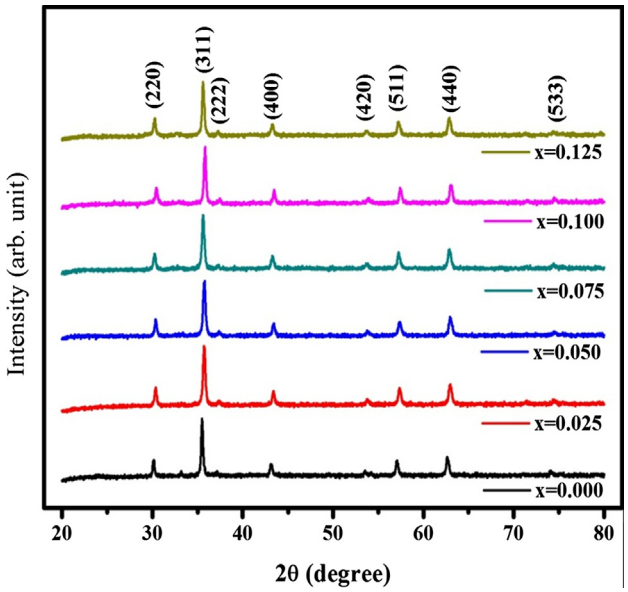

Fig. 2. XRD patterns of Sm^{3+} doped Ni-Co nanoferrites.

ferrite doped with trivalent rare earth ions for Fe^{3+} [13-15]. The substitution of large size rare earth ions in place of small size Fe^{3+} ions into the spinel structure leads to structural distortion and modulation in properties of ferrites [16,17]. Explicitly, the degree of modification in the properties of spinel ferrites depends on the size of ions, configuration of substituted ions, the occupancy of (A) or [B] site and the level of distribution at either (A) or [B] sites within the spinel structure [18,19]. The magnetic and dielectric properties of nanoferrites are strongly compelled to the distribution of the cations in the crystal structure [20].

Recently, the doping of rare earth ions for Fe^{3+} in spinel ferrites has received lot of weightage to prepare materials for storage devices and switching devices applications. Accordingly, researchers have investigated various characteristic properties of spinel ferrites substituted by trivalent rare earth ions for Fe^{3+} [21,22].

Incorporation of small quantity of ions into the spinel structure leads to the structural distortion which modulates various properties of prepared ferrite samples [23,24]. The modification in the properties of spinel ferrites depends on the radius of substituted ions, configuration of dopant ion, preference of site occupancy and the extent of distribution at the appropriate site within the spinel structure [25,26].

The structural and magnetic properties of spinel ferrites were simultaneously improved by substitution of rare earth ions like Gd, La, Ce and Dy [27,28]. The present study aims to investigate the impact of substitution of Sm^{3+} ions on structural, morphological and magnetic properties of $Ni_{0.5}$-$Co_{0.5}$ mixed spinel ferrite and their suitability for high frequency devices applications.

Table 1
Lattice constant (a), Crystallite Size (D), X-ray Density (d_X), Porosity (p), Lattice Strain (ε), Dislocation density (δ), Grain size (G) and Particles size (t).

Content x	a Å	D(nm) XRD	D(nm) W-H	Dx gm/cm^3	P(%)	ε %	δ lines/m^2	G Nm	t nm
0.000	8.342	33.38	32.61	5.366	33	0.190	8.9E+14	43	45
0.025	8.335	27.90	26.94	5.434	35.66	0.231	12E+14	44	49
0.050	8.324	25.58	25.57	5.510	47.33	0.252	15E+14	–	–
0.075	8.345	25.59	24.52	5.521	47.21	0.253	15E+14	–	–
0.100	8.321	30.91	29.97	5.624	40.73	0.208	10E+14	50	72
0.125	8.370	33.36	32.00	5.580	43.42	0.194	8.9E+14	47	52

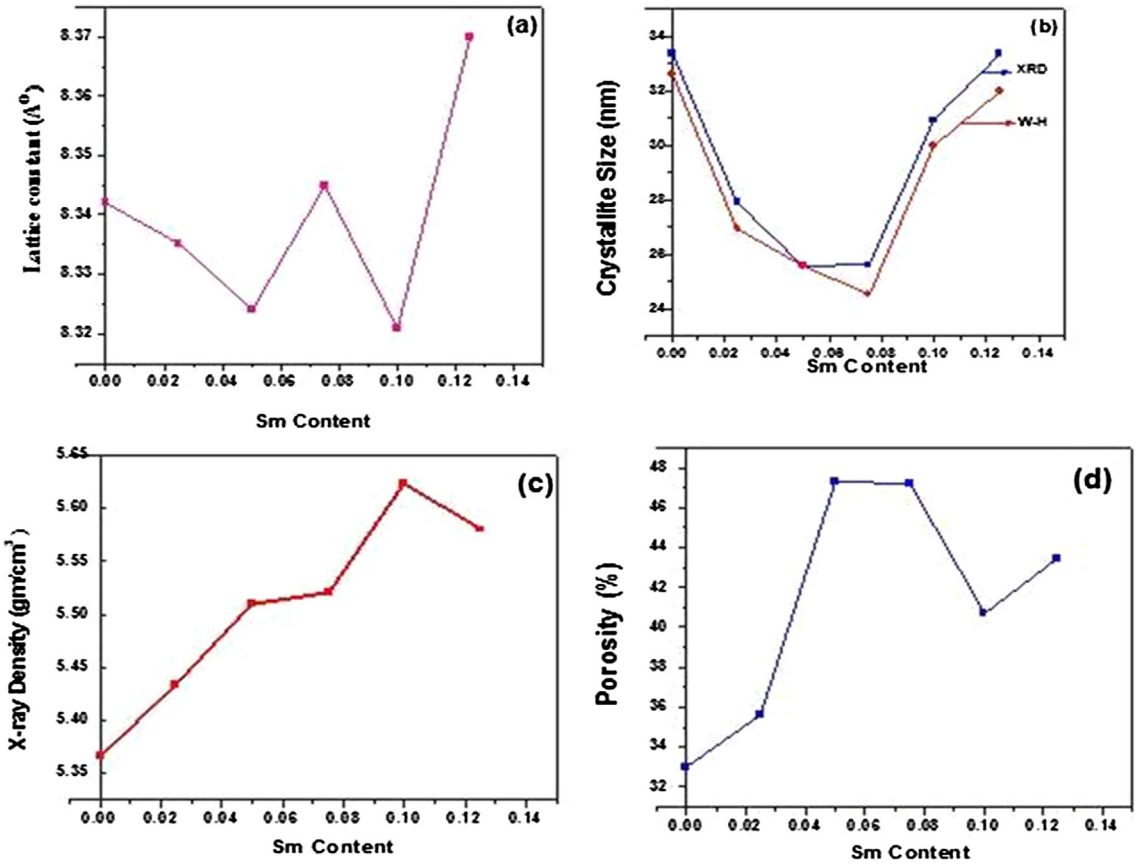

Fig. 3. Variation of (a) Lattice constant, (b) Crystallite size, (c) X-Ray Density, (d) Porosity with Sm^{3+} Content.

2. Experimental details

Nanocrystalline $Ni_{0.5}Co_{0.5}Sm_xFe_{2-x}O_4$ with x = 0.00, 0.025, 0.05, 0.075, 0.10, 0.125 samples were prepared by using auto-combustion route. Stoichiometric amounts of analytical grade $Co(NO_3)_2$ $6H_2O$, $Ni(NO_3)_2$ $6H_2O$, $Fe(NO_3)_3$ $9H_2O$, $Sm(NO_3)_3$ $6H_2O$ and citric acid were dissolved separately and mixed. The mixture was stirred for a few minutes to get a homogenous solution with heating upto 50 °C. Ammonia was added into the solution till the mixture becomes neutral. This solution was evaporated with continuous heating and stirring till the formation a continuous network of gel. The temperature was raised to 100 °C after the formation of gel which resulted in the fast flameless auto combustion reaction with the exhaust of fumes forming burned ash. This ash was grinded using agate pestle and mortar to get a fine ferrite powder. The samples in powder form were sintered at 700 °C for 4 h to get better crystallinity.

The structural characterization was performed by powder X-ray diffractometer (XRD) of Rigaku using Cu-Kα radiation (λ = 1.5405 Å). The morphology of samarium dopped Ni-Co ferrite samples was studied by scanning electron microscope JEOL (JEM-2010). The transmission electron microscope (TEM) PHILIPS (MODEL-CM 200) operating at 20–200 kV was employed to determinethe particle size and selected area electron diffraction (SAED) patterns. Vibrating sample magnetometer (Magenta Make) was used to measure magnetic properties of the prepared samples.

3. Results and discussion

3.1. TGA-DTA analysis

TGA-DTA curve of $Ni_{0.5}Co_{0.5}Sm_{0.1}Fe_{1.9}O_4$ is shown in Fig. 1.

Samples are decomposed in the range from 42 to 162 °C. The weight loss of 0.29 mg (1.44%) was observed in this range. This was due to evaporation of moisture from the sample.The second weight loss of 0.32 mg (1.85%) was observed for further decomposition in the range of 162–468 °C. The exothermic peak is observed at 410 °C which is shown by the DTA curve. The TGA curve shows that rate of weight loss is almost constant from the temperature of 622.47 °C. Accordingly the prepared samples were sintered at the temperature of 700 °C.

3.2. X-ray diffraction studies

Fig. 2 depicts the XRD patterns of the samarium ions substituted Ni-Co spinel ferrite nanoparticles of formula $Ni_{0.5}Co_{0.5}Sm_xFe_{2-x}O_4$ with (x = 0.0, 0.025, 0.05, 0.075, 0.10, 0.125) synthesized by sol-gel auto combustion technique. XRD patterns corresponding to all the compositions are indexed and reveal the cubic spinel structure. The XRD patterns show the reflections for peaks (2 2 0), (3 1 1), (2 2 2), (4 0 0), (4 2 2), (3 3 3) and (4 4 0) belonging to cubic spinel structure. All the diffraction peaks are well matched with those reported in the literature for spinel ferrite [29].

The XRD pattern analysis revealed that there is no evidence of secondary phase formation appeared. It has been reported in the literature that, when rare earth ion is doped in the spinel ferrite a secondary peak appeared [15,30]. In the present study, we have obtained single phase materials with rare earth Sm^{3+} ion doping. This can be attributed to the low-temperature synthesis of the samples using sol-gel auto combustion technique and the lower concentration of Sm^{3+} ions.

The values of the structural parameters for different compositions of Sm^{3+} are shown in Table 1. Using XRD data, the lattice parameter for each sample was calculated using the standard relation [31] and the values are tabulated in Table 1. It is observed that, the lattice constant decreased from 8.342 Å (x = 0) to 8.321 Å (x = 0.100) and increased for x = 0.125. The variation of lattice constant 'a' with the Sm^{3+}

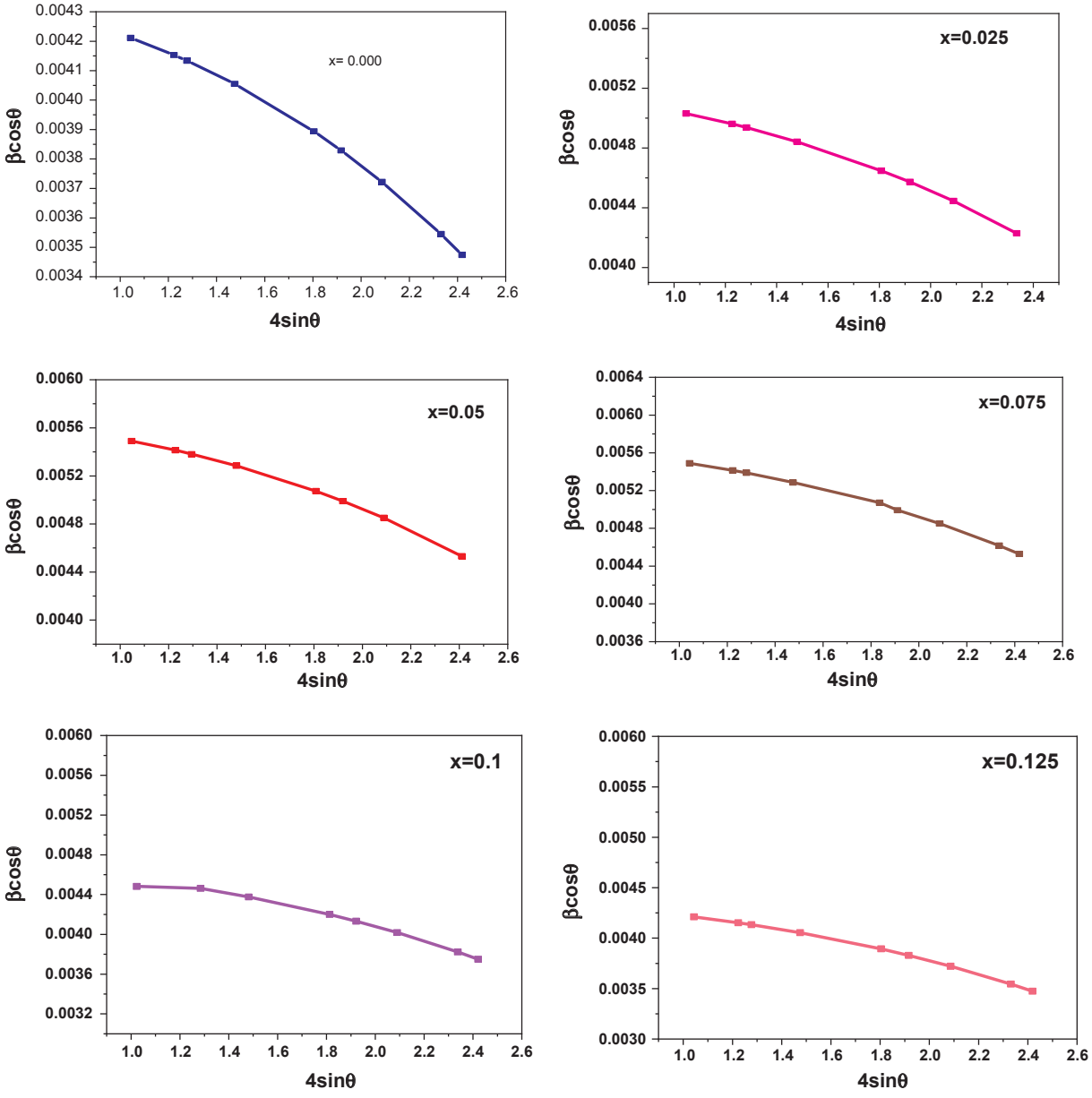

Fig. 4. W-H plots of $Ni_{0.5}Co_{0.5}Sm_xFe_{2-x}O_4$ nanoferrites.

content is shown in Fig. 3(a). Normally, the lattice constant increases with addition of rare earth doping which is owing to the difference in ionic radii of rare earth ion and Fe^{3+} ions [32]. However, in the present case, the lattice constant decreases with Sm^{3+} ion doping. The reason for the decrease in lattice constant may be the larger ionic radius of Sm^{3+} ions that leads to lattice distortion and results in the lower degree of alignments of lattice fringes [33]. The increase in lattice constant 8.370 Å (x = 0.125) may be due to the increase in the concentration of Sm^{3+} ions. The ionic radius of Sm^{3+} ion is greater than that of Fe^{3+} ion and hence lattice constant increases for x = 0.125. Many researchers attributed the non-linear variation of lattice constant to the distribution of cations [19,34,35]

The average crystallite size was calculated using the Scherrer equation which confirms the nanocrystalline nature of each sample. The average crystallite size for each composition as a function of Sm^{3+} ion concentration obtained from Scherrer formula and the crystallite size estimated from the W-H plots are tabulated in Table 1. Fig. 3(b) shows that both the values are in close agreement with each other. It can be seen from Table 1 that the crystallite size decreases up to x = 0.075 and rises with addition in Sm^{3+} content. Sm^{3+} ions are larger in size than Co, Ni and Fe ions, generally present at grain boundaries that limit growth and induce lattice strain resulting in to change in crystallite size and lattice parameter. Lattice strain increases with the concentration of samarium because of large radius of Sm^{3+} ions.

Table 1 shows that X-ray density increases from x = 0.00 to x = 0.10 and latter on it reduces for x = 0.125. The increase in X-ray density up to x = 0.10 is due to the larger molar mass of samarium. The molar mass of Sm is 144.25 gm/mole and that of Fe it is 55.84 gm/mole. The decrease in X-ray density for x = 0.125 is due to increase in lattice constant. Fig. 3(c) depicts the change in the value of x-ray density with the samarium composition.

The observations show that X-ray density is larger than bulk density for all the prepared samples. This is attributed to the existence of the pores that were formed during preparation and sintering of the samples. Fig. 3(d) shows that the porosity varies nonlinearly with increasing samarium composition. The porosity of Ni-Co nanoferrites ranges 33–47% for different composition of Sm content. This variation is

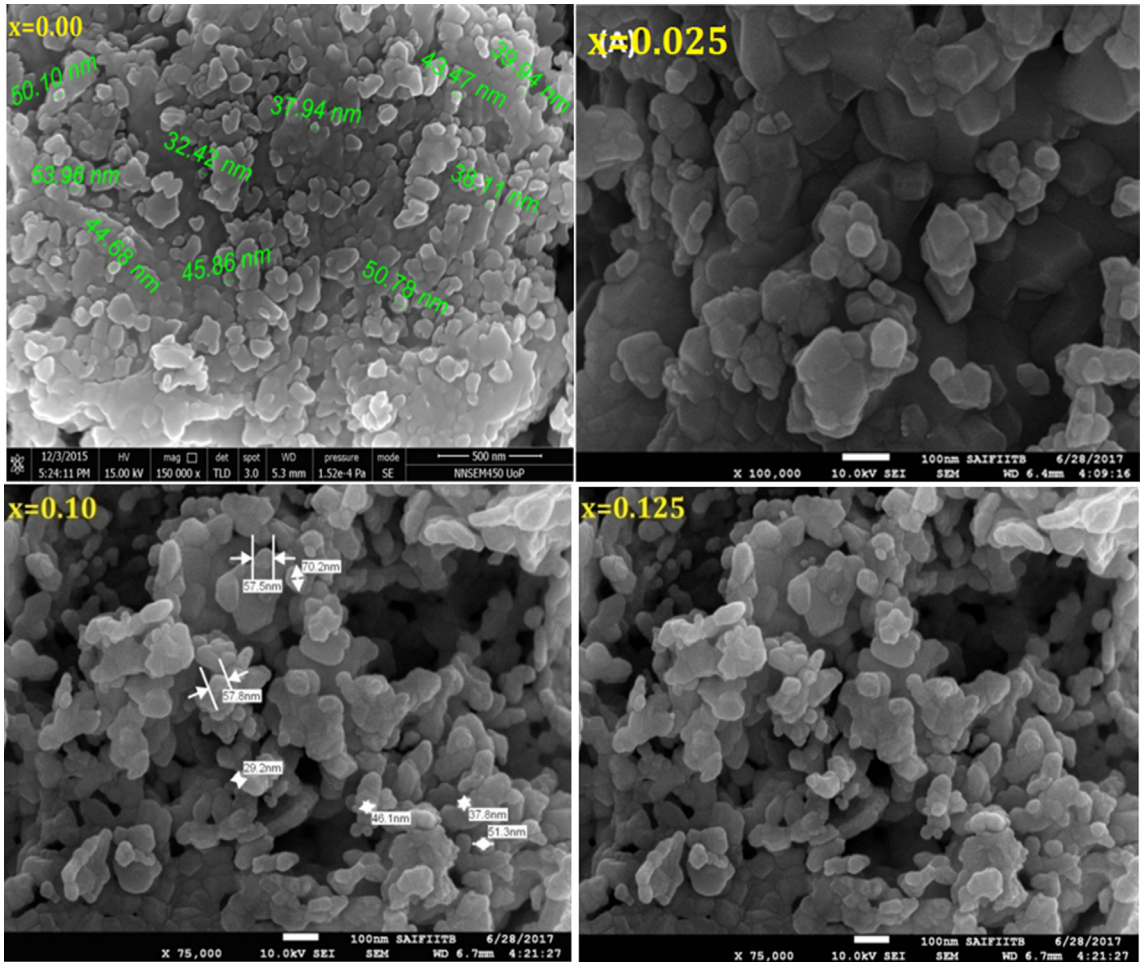

Fig. 5. FE-SEM images of $Ni_{0.5}Co_{0.5}Sm_xFe_{2-x}O_4$ (x = 0, 0.025, 0.1, 0.125).

attributed to change in occupancy of Sm^{3+} ions at (A) and [B] sites.

3.3. Williamson-Hall analysis

A Williamson–Hall analysis was performed by plotting a graph between βcosθ and 4sinθ for all prominent peaks. Crystallite size D is obtained by using the relation

$$D = \frac{\lambda}{\text{Intercept}} \quad (1)$$

Hall–Williamson plots of all the samples show a negative slope, which indicates a compressive strain on the particles when doped with Sm^{3+} ions of a large ionic radius when compared to Fe^{3+}.

Williamson-Hall plots drawn for all the prepared samples are shown in Fig. 4. The lattice strain was increased with Sm^{3+} doping up to x = 0.075 and decreases for x ≥ 0.10. The variation in lattice strain is due to the change in dislocations, micro stresses, grain boundaries, coherency stresses and crystallite smallness. In the present case, the dislocation density (δ) increases up to x = 0.075 and then reduces with Sm^{3+} ion concentration, the crystallite size of all the samples are small and therefore lattice strain is induced in the prepared samples.

3.4. FE-SEM analysis

The FE-SEM micro images of the $Ni_{0.5}Co_{0.5}Sm_xFe_{2-x}O_4$ (x = 0.0, 0.025, 0.1, 0.125) ferrites are shown in Fig. 5. It represents the typical scanning electron micrographs of $Ni_{0.5}Co_{0.5}Sm_xFe_{2-x}O_4$x = 0.00, 0.025, 0.10 and 0.125 samples. The surface morphology of $Ni_{0.5}Co_{0.5}Sm_xFe_{2-x}O_4$ shows spherical shaped grains with good homogeneity as shown in Fig. 5.

The micrographs show the agglomerated grain structure which is attributed to interaction between magnetic nanoparticles [36]. The average grain size obtained from SEM micrograph is given in Table 2 and is found larger than the crystallite size. This indicates that the large number of crystallites aggregates and particles are formed. Also, this may be due to the agglomeration of the particles during processing of the samples. The analysis of FE-SEM images show that the grain size increases from 43 (x = 0.0) to 50 (x = 0.1) and then decreases up to 47 (x = 0.125). The magnitude of grain size proves that prepared samples are nanocrystalline in nature.

The elemental composition of $Ni_{0.5}Co_{0.5}Sm_xFe_{2-x}O_4$ samples (x = 0.0, 0.025, 0.1 and 0.125) was studied by energy dispersive X-ray spectrometer attached with FE-SEM. Fig. 6 shows typical EDS spectra of $Ni_{0.5}Co_{0.5}Sm_xFe_{2-x}O_4$ samples for (x = 0.0, 0.025, 0.1 and 0.125). It revealed the presence of Co, Ni, Fe, O and Sm^{3+} and do not contain any other elements. This indicates the fact that the prepared samples of $Ni_{0.5}Co_{0.5}Sm_xFe_{2-x}O_4$ are pure without any impurity.

3.5. TEM analysis

Average particle size estimated from TEM images is shown in Table 1. The crystalline nature of spinel phase was confirmed by position of diffraction rings corresponding to SAED pattern. TEM images of the $Ni_{0.5}Co_{0.5}Sm_xFe_{2-x}O_4$ for (x = 0.00, 0.025, 0.1 and 0.125) samples along with selected area electron diffraction (SAED) patterns and histogram are shown in Fig. 7. The dots in diffraction rings confirms that

Table 2
Elemental composition of$Ni_{0.5}Co_{0.5}Sm_xFe_{2-x}O_4$ (x = 0, 0.025, 0.1, 0.125).

Element	Weight%	Atomic%
O K	24.00	52.88
Fe K	48.82	30.82
Co K	15.38	9.20
Ni K	11.80	7.10
Nd L	0.00	0.00
Sm L	0.00	0.00
Totals	100.00	100.00

x = 0

Element	Weight%	Atomic%
O K	17.31	44.28
Fe K	49.51	36.29
Co K	12.81	8.90
Ni K	11.75	8.19
Nd L	0.00	0.00
Sm L	8.62	2.35
Totals	100.00	100.01

x = 0.025

Element	Weight%	Atomic%
O K	22.32	50.95
Fe K	49.05	32.07
Co K	13.22	8.19
Ni K	13.30	8.27
Nd L	0.00	0.00
Sm L	2.11	0.51
Totals	100.00	99.99

x = 0.1

Element	Weight%	Atomic%
O K	24.68	55.23
Fe K	44.01	28.21
Co K	12.66	7.69
Ni K	11.92	7.27
Nd L	0.00	0.00
Sm L	6.73	1.60
Totals	100.00	100.00

x = 0.125

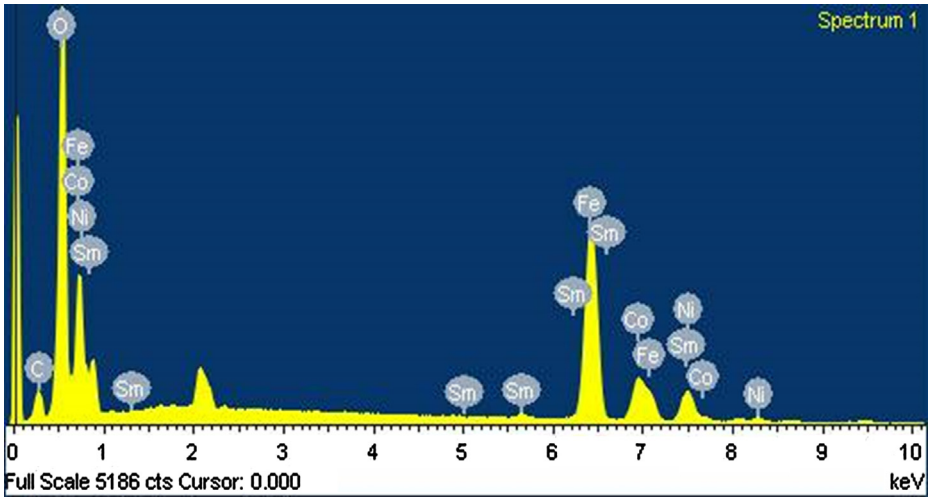

Fig. 6. Elemental composition and EDS patterns of $Ni_{0.5}Co_{0.5}Sm_xFe_{2-x}O_4$.

the long range of nanoferrites, due to regular packing of small mono crystalline particles in different orientations [37]. The TEM micrographs show that the most of the nanoparticles are spherical in shape and are agglomerated [38]. The average particle size of $Ni_{0.5}Co_{0.5}Sm_xFe_{2-x}O_4$ samples determined from TEM images was found to be 45 nm, 49 nm, 72 nm and 52 nm for x = 0.0, 0.025, 0.1 and 0.125 respectively.

The particle size of the samples estimated from TEM technique is slightly larger than the crystallite size and the grain size. This difference is due to the agglomeration of nanocrystalline ferrites.

3.6. FTIR analysis

The FTIR spectra of $Ni_{0.5}Co_{0.5}Sm_xFe_{2-x}O_4$ samples recorded over

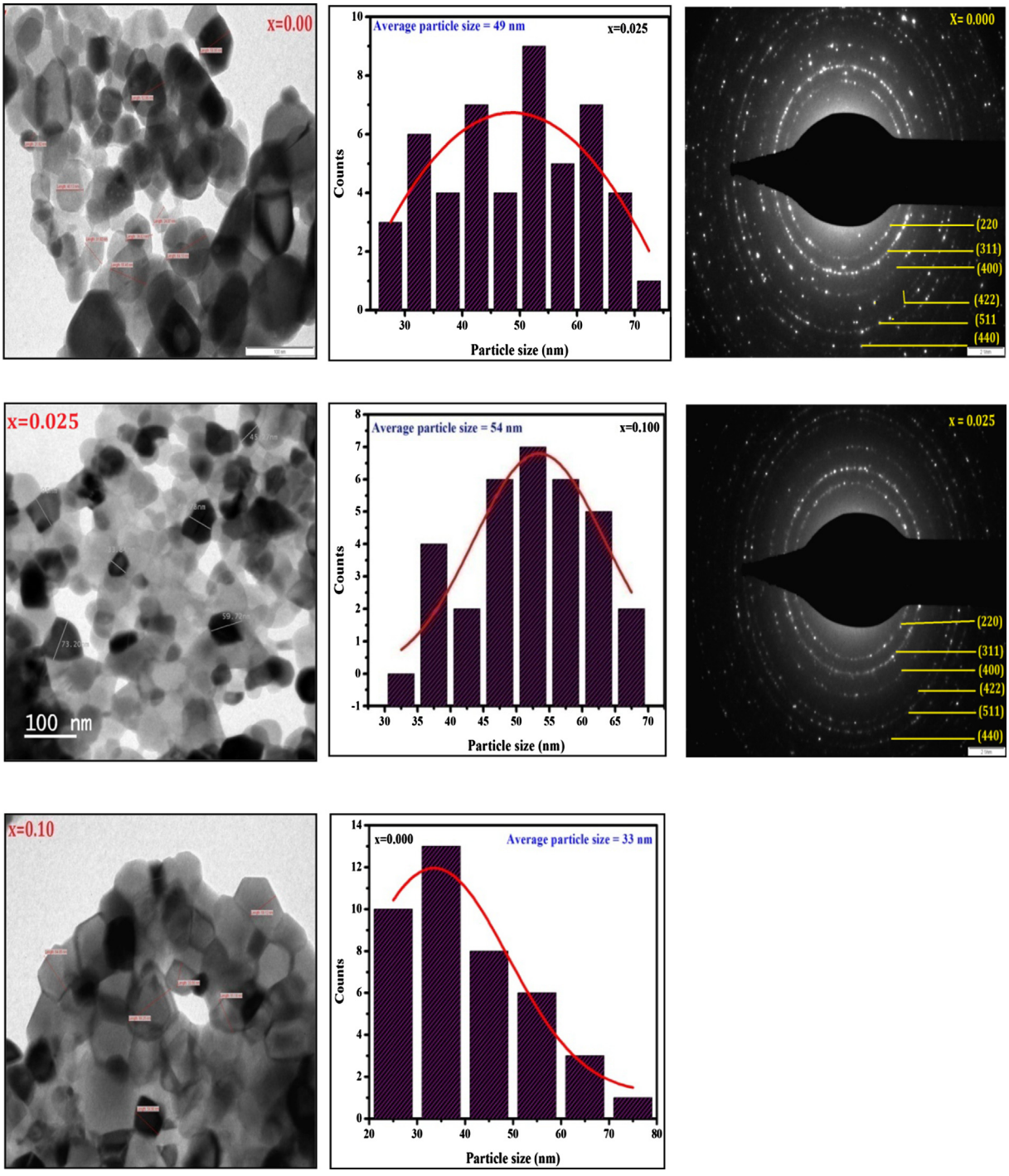

Fig. 7. TEM mages, Histogram and SAED pattern. (x = 0, 0.025 and 0.10).

the range of 400–4000 cm^{-1} are shown in Fig. 8. Ferrite shows two prominent metal-oxygen frequencies. The higher frequency band ν_1 and lower frequency band ν_2 were detected in the range of 552–465 cm^{-1} and 425–400 cm^{-1} and was assigned to (A) and [B] sites metal stretching, which are considered to be the typical bands of spinel structure [32]. The values of absorption frequency ν_1 and ν_2 are listed in Table 3.This can be due to shifting of Fe^{3+} ions along oxygen ion on the tetrahedral site which decreases with Fe^{3+}-O^{2-} distance. The fundamental frequency was reduced and central frequency was shifted towards the lower side due to increase in site radius.

3.7. Magnetic properties

The magnetic measurements of $Ni_{0.5}Co_{0.5}Sm_xFe_{2-x}O_4$ (x = 0, 0.025, 0.05, 0.075, 0.10, 0.125) samples were carried out by VSM at room temperature and the M−H curves are shown in Fig. 9. The magnetic parameters viz. saturation magnetization, remanence magnetization, and coercivity were determined from M−H curves and the values are tabulated in Table 4. It indicates the decrease in saturation magnetization and remanence magnetization with Sm^{3+} ions substitution excluding x = 0.1. This can be described with the substitution of Fe^{3+} ($5\mu_B$) ions by rare earth ions possessing smaller magnetic moment of Sm^{3+} ($3\mu_B$). On the other hand, if magnetic moment of rare

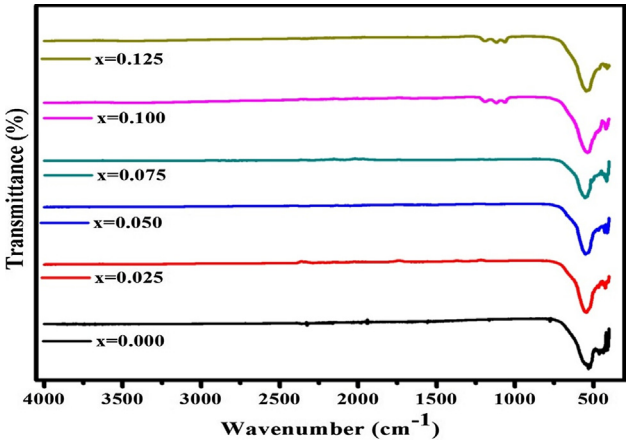

Fig. 8. FTIR Spectra of $Ni_{0.5}Co_{0.5}Sm_xFe_{2-x}O_4$ nanoferrites.

Table 3
FTIR Absorption frequency bands.

Composition (x)	ν_1 cm^{-1}	ν_2 cm^{-1}
0	400	465
0.025	422	543
0.05	411	548
0.075	415	552
0.1	419	538
0.125	411	544

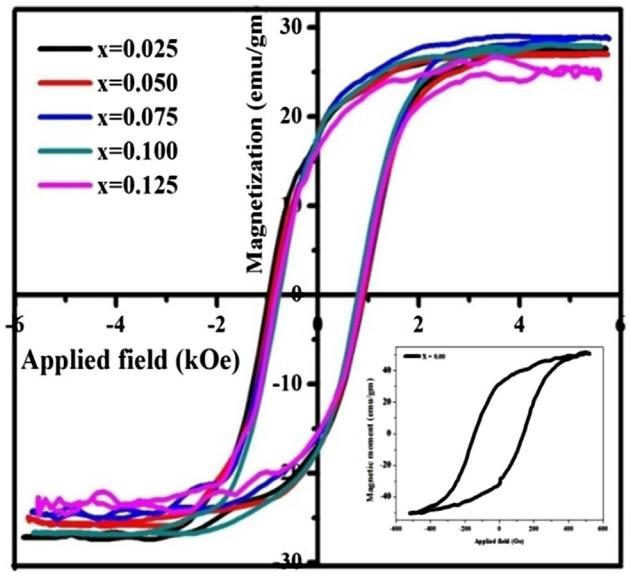

Fig. 9. M − H plots of $Ni_{0.5}Co_{0.5}Sm_xFe_{2-x}O_4$.

Table 4
Magnetic parameters Ms, Mr, Mr/Ms, Hc and n_B.

Composition X	Ms (emu/gm)	Mr (emu/gm)	R = Mr/Ms	Hc (Oe)	n_B
0	51.85	31.75	0.61	1396.02	2.1773
0.025	28.46	20.00	0.70	977.11	1.1787
0.050	27.68	19.74	0.71	874.59	1.1650
0.075	26.73	17.87	0.66	855.37	1.1428
0.10	27.50	19.04	0.69	794.50	1.2013
0.125	25.00	16.08	0.64	823.34	1.1027

earth ion is greater than that of Fe^{3+} then the situation is reversed. But this behavior is not shown by all rare earth ions substituted ferrites. Reports indicate that the rare earth ions prefer to occupy octahedral [B] site when doped in ferrites [21,22]. In this study it is observed that, all the magnetic parameters decreased from x = 0.0 to 0.125 with increasing Sm^{3+} content. This decrease is attributed to the substitution of Sm^{3+} ions having low magnetic moment ($3\mu_B$) in place of Fe^{3+} ions of large magnetic moment ($5\mu_B$) [23].

The variation of saturation magnetization and remenance magnetization as a function of Sm^{3+} content x is depicted in Fig. 10(a) and (b). It can be observed from Fig. 10(a) and (b) that the saturation magnetization and remenance magnetization decreases from x = 0.00 to x = 0.075. For x = 0.100 it slightly increases and again decreases for x = 0.125. In spinel ferrites, the arrangement between A-A and B-B is parallel whereas the arrangement between A-B is anti-parallel which give an ordering arrangement of ferrimagnetism. Usually, the ions of larger ionic radii are supposed to occupy octahedral sites. Thus, the rare earth ions like Sm^{3+} ions occupy octahedral site by replacing Fe^{3+} ions [24]. Magnetic properties possessed by the spinal ferrites are mainly contributed by Fe^{3+} situated at [B] sites of spinel ferrite. The magnetic moment of Sm^{3+} ions is less than that of Fe^{3+} ions, so the super-exchange interaction may decrease significantly with the substitution of Sm^{3+} ions. However, it is observed that both the Ms and Mr increases from x = 0.075 to x = 0.1. At this composition the increase in content of Sm^{3+} ions forces Ni^{2+} ions to move from octahedral site to tetrahedral site. Further, it decreases from x = 0.1 to x = 0.125. This may be due to shifting of Ni^{2+} from tetrahedral to octahedral site. Nickel ferrite is a partially inverse spinel ferrite $(Ni_{0.05}Fe_{0.95})^A[Ni_{0.95}Fe_{1.05}]^B O_4$, while cobalt ferrite is a perfect inverse spinel ferrite $(Fe_1)^A[Co_1Fe_1]^BO_4$. Ni^{2+} ions have a tendency to occupy tetrahedral site and can easily push from octahedral site to tetrahedral site. This results in the increase in saturation magnetization. The magneton number (n_B) of the prepared ferrites was obtained by the relation [39].

$$n_B = M \times M_s/5585 \quad (2)$$

where M is mol. wt. of a particular ferrite content and Ms is a saturation magnetization in emu/gm. The observed magnetic behaviour of the doped nanoferrites is explained on the basis of Neel's model [25]. Neel's magnetic moment is given by $n_B = M_B - M_A$, where M_B is a magnetic moment of B sub-lattice and M_A is magnetic moment of A sub-lattice. The spinel crystal structure consists of two interstitial sites (A) and [B] site. Out of these interstitial sites, the inter sub-lattice A-B super exchange interaction and intra sub-lattice A-A and B-B superexchange interaction exits. Interaction between A-B ions is much stronger than the A-A and B-B interactions.

Table 4 shows that the coercivity decreases from x = 0 to x = 0.1 and then increases for x = 0.125. The variation in coercivity with the composition x is shown in Fig. 10(c). The substitution of Sm^{3+} ions lead to alteration in magneto-crystalline anisotropy (K) which is due to the difference in the magneto-crystalline anisotropy constant of Sm^{3+}, Ni^{2+} and Co^{2+}. Thus, substitution of Sm^{3+} ions reduces the coercivity of the present samples.

4. Conclusions

A series of Sm^{3+} doped Ni-Co spinal ferrite were successfully synthesized by the sol-gel auto-combustion method. XRD pattern analysis confirmed the single-phase cubic spinel structure with no evidence of secondary phase. The crystallite size and particle size indicate the nano sized nature of the prepared ferrites. The agglomerated grain structure revealed the high surface interaction between magnetic nanoparticles. FTIR spectra revealed the characteristics features of ferrite skeleton formation. The saturation magnetization, coercivity and remanence magnetization were found to decreases with the substitution of Sm^{3+} ions. The decrease in magnetic properties with substitution of Sm^{3+} shows soft ferromagnetic behavior suitable for recording and storage

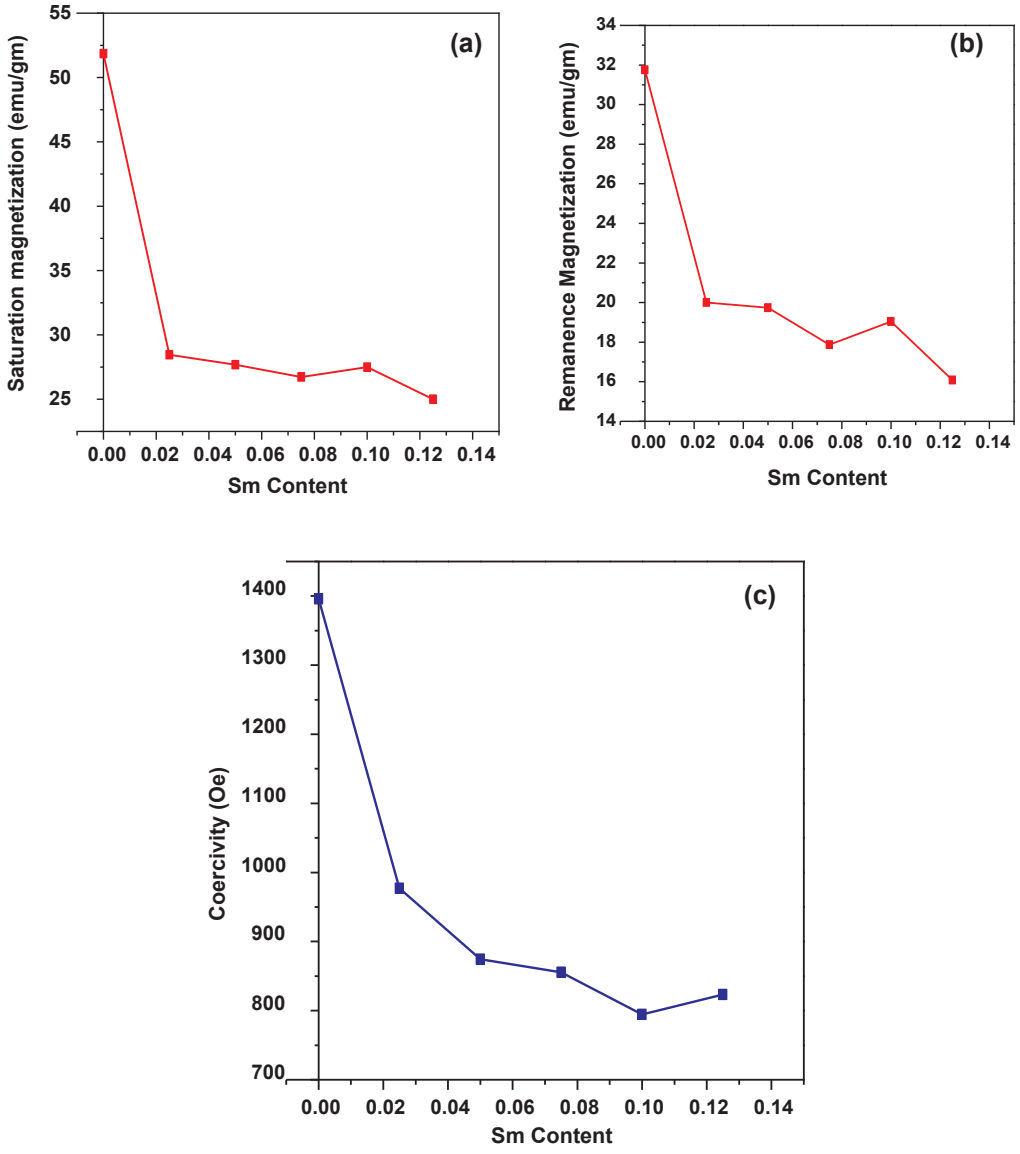

Fig. 10. Variation of (a) Ms (b) Mr and (c) Hc with Sm^{3+} Content.

devices applications.

Acknowledgment

Authors are very much thankful to Tuljaram Chaturchand College, Baramati and Post –Graduate and Research Centre, Abasaheb Garware College, Pune, for providing research facilities.

Author states that this research work has not been financially supported by any funding agency.

References

[1] I.H. Gul, A. Maqsood, J. Alloys Compd. 465 (2008) 227–231.
[2] P. Kumar, S.K. Sharma, M. Knobel, M. Singh, J. Alloys Compd. 508 (2010) 115–118.
[3] A. Raghavender, D. Pajic, K. Zadro, T. Milekovic, P.V. Rao, K. Jadhav, D. Ravinder, J. Magn. Magn. Mater. 316 (2007) 1–7.
[4] J.M. De Vidales, A. Lopez-Delgado, E. Vila, F. Lopez, J. Alloys Compd. 287 (1999) 276–283.
[5] V. Mathe, R. Kamble, Mater. Res. Bull. 43 (2008) 2160–2165.
[6] V. Mathe, A. Sheikh, Physica B: Condens. Matter 405 (2010) 3594–3598.
[7] B. Chauhan, R. Kumar, K. Jadhav, M. Singh, J. Magn. Magn. Mater. 283 (2004) 71–81.
[8] S. Patange, S.E. Shirsath, G. Jangam, K. Lohar, S.S. Jadhav, K. Jadhav, J. Appl. Phys. 109 (2011) 053909.
[9] B.M. Sahanashree, E. Melagiriyappa, M. Veena, G.J. Shankaramurthy, H.M. Somashekarappa, Mater. Chem. Phys. 214 (2018) 143–153.
[10] V. Mathe, R. Kamble, Mater. Res. Bull. 48 (2013) 1415–1419.
[11] S.J. Santosh, E.S. Sagar, B. Toksha, S. Shukla, K. Jadhav, Chin. J. Chem. Phys. 21 (2008) 381.
[12] S.E. Shirsath, S.S. Jadhav, B. Toksha, S. Patange, K. Jadhav, Scripta Materialia 64 (2011) 773–776.
[13] S.E. Shirsath, B. Toksha, K. Jadhav, Mater. Chem. Phys. 117 (2009) 163–168.
[14] S. Patange, S.E. Shirsath, B. Toksha, S.S. Jadhav, K. Jadhav, J. Appl. Phys. 106 (2009) 023914.
[15] S. Naik, A. Salker, J. Mater. Chem. 22 (2012) 2740–2750.
[16] Z. Karimi, Y. Mohammadifar, H. Shokrollahi, S.K. Asl, G. Yousefi, L. Karimi, J. Magn. Magn. Mater. 361 (2014) 150–156.
[17] S. Amiri, H. Shokrollahi, J. Magn. Magn. Mater. 345 (2013) 18–23.
[18] F.L. Deepak, M. Bañobre-López, E. Carbó-Argibay, M.F.t. Cerqueira, Y. Piñeiro-Redondo, J. Rivas, C.M. Thompson, S. Kamali, C. Rodríguez-Abreu, K. Kovnir, J. Phys. Chem. C 119 (2015) 11947–11957.
[19] V.L. Deringer, C. Goerens, M. Esters, R. Dronskowski, B.P. Fokwa, Chemical modeling of mixed occupations and site preferences in anisotropic crystal structures: case of complex intermetallic borides, Inorg. Chem. 51 (2012) 5677–5685.
[20] B. Parvatheeswara Rao, B. Dhanalakshmi, S. Ramesh, P.S.V. Subba Rao, Cationdistribution of Ni-Zn-Mn ferrite nanoparticles, J. Magn. Magn. Mater. 456 (2018) 444–450.
[21] F.-X. Cheng, J.-T. Jia, Z.-G. Xu, B. Zhou, C.-S. Liao, C.-H. Yan, L.-Y. Chen, H.-B. Zhao, J. Appl. Phys. 86 (1999) 2727–2732.
[22] S. Jacobo, S. Duhalde, H. Bertorello, J. Magn. Magn. Mater. 272 (2004) 2253–2254.
[23] A. Gadkari, T. Shinde, P. Vasambekar, Mater. Chem. Phys. 114 (2009) 505–510.
[24] L.B. Tahar, M. Artus, S. Ammar, L. Smiri, F. Herbst, M.-J. Vaulay, V. Richard, J.-

M. Grenèche, F. Villain, F. Fievet, J. Magn. Magn. Mater. 320 (2008) 3242–3250.
[25] A. Nikumbh, R. Pawar, D. Nighot, G. Gugale, M. Sangale, M. Khanvilkar, A. Nagawade, J. Magn. Magn. Mater. 355 (2014) 201–209.
[26] J. Liu, C.G. Duan, W.G. Yin, W.N. Mei, R.W. Smith, J.R. Hardy, Physical Review B 70 (2004) 144106.
[27] F. Cheng, C. Liao, J. Kuang, Z. Xu, C. Yan, L. Chen, H. Zhao, Z. Liu, J. Appl. Phys. 85 (1999) 2782–2786.
[28] G. Dascalu, G. Pompilian, B. Chazallon, V. Nica, O.F. Caltun, S. Gurlui, C. Focsa, Appl. Phys. A 110 (2013) 915–922.
[29] S.G. Kakade, R.C. Kambale, K. Kolekar, C.V. Raman, J. Phys. Chem. C 113 (2016) 9070–9076.
[30] E. Mazario, N. Menendez, P. Herrasti, M. Canete, V. Connord, J. Carrey, J. Phys. Chem. C 11 (2013) 1105–11411.
[31] B.D. Cullity, J.W. Weymouth, Elements of X-ray Diffraction, Am. J. Phys. 25 (1957) 394–395.
[32] M. Farid, I. Ahmad, S. Aman, M. Kanwal, G. Murtaza, I. Ali, I. Ahmad, M. Ishfaq, Dig. J. Nanomater. Biostruct. 10 (2015) 265–275.
[33] E. Ateia, M. Ahmed, A. El-Aziz, J. Magn. Magn. Mater. 311 (2007) 545–554.
[34] K.K. Bamzai, B. GurbinderKour, S.D. Kaur, Kulkarni, J. Magn. Magn. Mater. 327 (2013) 159–166.
[35] M. Arana, V. Galván, S.E. Jacobo, P.G. Bercoff, Cation distribution and magnetic properties of LiMnZn ferrites, J. Alloys Compd. 568 (2013) 5–10.
[36] Z.K. Heiba, A.M. Wahba, M.B. Mohamed, J. Mol. Struct. 1147 (2017) 668–675.
[37] N. Najmoddin, A. Beitollahi, E. Devlin, H. Kavas, S.M. Mohseni, J. Åkerman, D. Niarchos, H. Rezaie, M. Muhammed, M.S. Toprak, Micropor. Mesopor. Mater. 190 (2014) 346–355.
[38] Md.T. Rahman, M. Vargas, C.V. Ramana, J. Alloys Compd. 617 (2014) 547–562.
[39] B.V. Rao, A.D.P. Rao, Influence of Mo6+ on magnetic and micro-structural properties of copper ferrite, J. Alloys Compd. 708 (2017) 141–145.